

Supplementary File-LIGO: A Tightly Coupled LiDAR-Inertial-GNSS Odometry based on a Hierarchy Fusion Framework for Global Localization with Real-time Mapping

Dongjiao He¹, Haotian Li¹, Jie Yin²

I. ILLUSTRATION OF THE SINGLE PRECISE POSITION ALGORITHM

The illustration figure for the Single Precise Position Algorithm is shown as in Fig. 1.

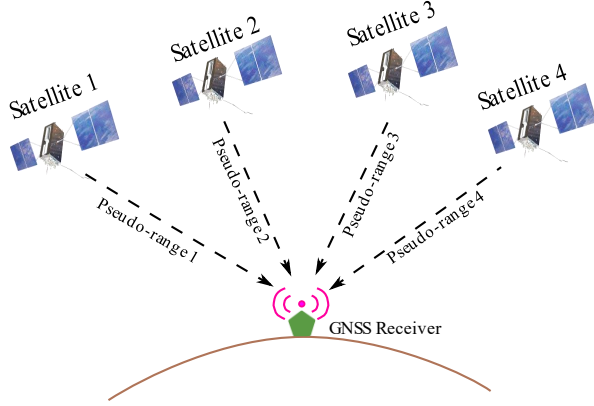


Fig. 1. Illustration of the SPP algorithm, where several (more than 4) pseudo-range measurements are used to solve the position of the GNSS receiver in the ECEF coordinate and the receiver's clock offsets.

II. CALCULATION OF THE JACOBIAN MATRICES OF HATCH FILTER AND DOPPLER SHIFTS WITH RESPECT TO THE GNSS RECEIVER POSITION

To solve the respective constraint directions of the Hatch filter (\mathcal{C}_h) and the Doppler shifts (\mathcal{C}_d) for the position estimation, we calculate the Jacobian matrices of equations (7) and (8) in the manuscript with respect to the position ${}^w\mathbf{p}_k$ [1], as follows:

$$\begin{aligned}\mathcal{C}_h &= \frac{\partial \mathbf{r}(\mathcal{X}_k, \mathbf{z}_k^h)}{\partial {}^w\mathbf{p}_k} = \frac{({}^E\mathbf{T}_{k_i}^w \mathbf{p}_k - {}^E\mathbf{p}_k^j)^T}{\|{}^E\mathbf{p}_k^j - {}^E\mathbf{T}_{k_i}^w \mathbf{p}_k\|} {}^E\mathbf{T}_{k_i}^w \\ \mathcal{C}_d &= \frac{\partial \mathbf{r}(\mathcal{X}_k, \mathbf{z}_k^d)}{\partial {}^w\mathbf{p}_k} \\ &= \frac{({}^E\mathbf{v}_k^j - {}^E\mathbf{R}_{k_i}^w \mathbf{v}_k)^T}{\|{}^E\mathbf{p}_k^j - {}^E\mathbf{T}_{k_i}^w \mathbf{p}_k\|} \\ &\quad \cdot \left(\mathbf{I} - \frac{({}^E\mathbf{p}_k^j - {}^E\mathbf{T}_{k_i}^w \mathbf{p}_k)({}^E\mathbf{p}_k^j - {}^E\mathbf{T}_{k_i}^w \mathbf{p}_k)^T}{\|{}^E\mathbf{p}_k^j - {}^E\mathbf{T}_{k_i}^w \mathbf{p}_k\|^2} \right) {}^E\mathbf{T}_{k_i}^w \\ &= \alpha \frac{({}^E\mathbf{v}_k^j - {}^E\mathbf{R}_{k_i}^w \mathbf{v}_k)^T}{\|{}^E\mathbf{v}_k^j - {}^E\mathbf{R}_{k_i}^w \mathbf{v}_k\|} {}^E\mathbf{T}_{k_i}^w - \beta \frac{({}^E\mathbf{p}_k^j - {}^E\mathbf{T}_{k_i}^w \mathbf{p}_k)^T}{\|{}^E\mathbf{p}_k^j - {}^E\mathbf{T}_{k_i}^w \mathbf{p}_k\|} {}^E\mathbf{T}_{k_i}^w\end{aligned}\quad (1)$$

where

$$\begin{aligned}\alpha &= \frac{\|{}^E\mathbf{v}_k^j - {}^E\mathbf{R}_{k_i}^w \mathbf{v}_k\|}{\|{}^E\mathbf{p}_k^j - {}^E\mathbf{T}_{k_i}^w \mathbf{p}_k\|} \\ \beta &= \frac{({}^E\mathbf{v}_k^j - {}^E\mathbf{R}_{k_i}^w \mathbf{v}_k)^T ({}^E\mathbf{p}_k^j - {}^E\mathbf{T}_{k_i}^w \mathbf{p}_k)}{\|{}^E\mathbf{p}_k^j - {}^E\mathbf{T}_{k_i}^w \mathbf{p}_k\|^2}\end{aligned}\quad (2)$$

¹The authors are with Department of Mechanical Engineering, University of Hong Kong. {hdj65822, haotianli}@connect.hku.hk

²The author is with Department of Electronic Engineering, Shanghai Jiao Tong University. 594666@sjtu.edu.cn

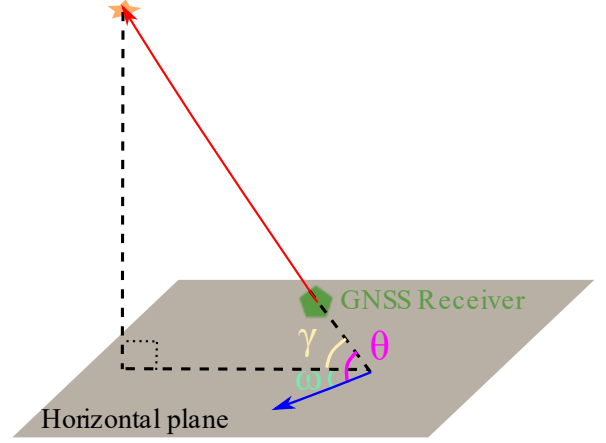


Fig. 2. Illustration of the intersection angle between the vector $\frac{{}^E\mathbf{v}_k^j - {}^E\mathbf{R}_{k_i}^w \mathbf{v}_k}{\|{}^E\mathbf{v}_k^j - {}^E\mathbf{R}_{k_i}^w \mathbf{v}_k\|}$ (in blue) and the vector $\frac{{}^E\mathbf{p}_k^j - {}^E\mathbf{T}_{k_i}^w \mathbf{p}_k}{\|{}^E\mathbf{p}_k^j - {}^E\mathbf{T}_{k_i}^w \mathbf{p}_k\|}$ (in red).

and the other symbols are defined in the equations (7) and (8) of the manuscript.

Moreover, β is related to the α as:

$$\begin{aligned}\beta &= \frac{({}^E\mathbf{v}_k^j - {}^E\mathbf{R}_{k_i}^w \mathbf{v}_k)^T ({}^E\mathbf{p}_k^j - {}^E\mathbf{T}_{k_i}^w \mathbf{p}_k)}{\|{}^E\mathbf{p}_k^j - {}^E\mathbf{T}_{k_i}^w \mathbf{p}_k\|^2} \\ &= \frac{\|{}^E\mathbf{v}_k^j - {}^E\mathbf{R}_{k_i}^w \mathbf{v}_k\|}{\|{}^E\mathbf{p}_k^j - {}^E\mathbf{T}_{k_i}^w \mathbf{p}_k\|} \cdot \frac{({}^E\mathbf{v}_k^j - {}^E\mathbf{R}_{k_i}^w \mathbf{v}_k)^T ({}^E\mathbf{p}_k^j - {}^E\mathbf{T}_{k_i}^w \mathbf{p}_k)}{\|{}^E\mathbf{v}_k^j - {}^E\mathbf{R}_{k_i}^w \mathbf{v}_k\| \|{}^E\mathbf{p}_k^j - {}^E\mathbf{T}_{k_i}^w \mathbf{p}_k\|} \\ &= \alpha \cdot \cos(\theta)\end{aligned}\quad (3)$$

where θ is the intersection angle of two normalized vectors: $\frac{{}^E\mathbf{v}_k^j - {}^E\mathbf{R}_{k_i}^w \mathbf{v}_k}{\|{}^E\mathbf{v}_k^j - {}^E\mathbf{R}_{k_i}^w \mathbf{v}_k\|}$ and $\frac{{}^E\mathbf{p}_k^j - {}^E\mathbf{T}_{k_i}^w \mathbf{p}_k}{\|{}^E\mathbf{p}_k^j - {}^E\mathbf{T}_{k_i}^w \mathbf{p}_k\|}$. The first vector is almost aligned with the satellite velocity direction, since the velocity of the GNSS receiver, i.e., ${}^E\mathbf{R}_{k_i}^w \mathbf{v}_k$, is negligible as compared with the satellite velocity. The second vector points from the receiver position to the satellite position.

Assuming the direction of the satellite velocity is parallel to the horizontal plane of the Earth as stated in the manuscript and denoting the elevation angle as γ as defined in the manuscript, we have

$$|\cos(\theta)| = |\cos(\gamma)| \cdot |\cos(\omega)| \leq |\cos(\gamma)| \quad (4)$$

where ω is the angle between the $\frac{{}^E\mathbf{v}_k^j - {}^E\mathbf{R}_{k_i}^w \mathbf{v}_k}{\|{}^E\mathbf{v}_k^j - {}^E\mathbf{R}_{k_i}^w \mathbf{v}_k\|}$ and the vector within the horizontal plane projected by the $\frac{{}^E\mathbf{p}_k^j - {}^E\mathbf{T}_{k_i}^w \mathbf{p}_k}{\|{}^E\mathbf{p}_k^j - {}^E\mathbf{T}_{k_i}^w \mathbf{p}_k\|}$, as illustrated in Fig. 2.

III. DETAILED EXPERIMENT RESULTS OF THE DEG-2 SEQUENCE

In this experiment, the UAV embarked on a more arbitrary flight path. Starting from a flat area amidst the forest with

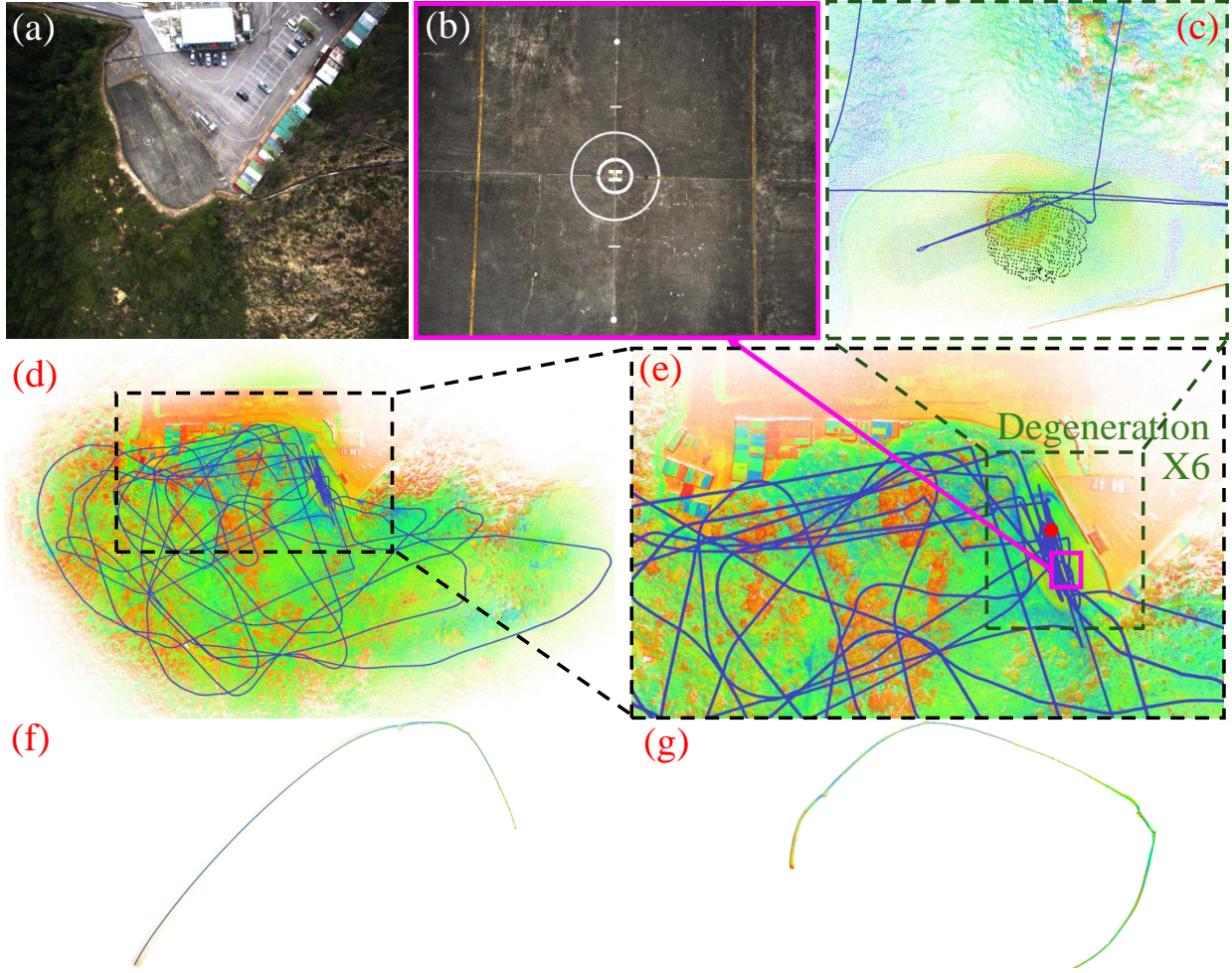


Fig. 3. Mapping results of LIGO (c)-(e), LIGO-loosely (f), and Point-LIO (g) on the Deg-2 sequence. Red dot in (e) marks the starting point of the trajectory. In the area boxed in pink in (e), LiDAR degenerates by directing to a flat ground (b). (c) shows the current LiDAR scan in black when scanning the flat floor. The UAV comes to this flat area 6 times. LIGO-loosely (f) and Point-LIO (g) diverge due to the degeneracy at the beginning of the sequence.

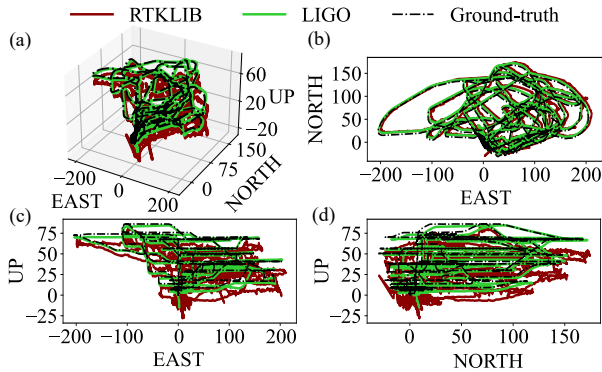


Fig. 4. Comparisons of trajectory estimations after the initial 50s of LIGO, RTKLIB, and ground truth on Deg-2 sequence. Due to the severe degeneracy, all the LIGO-loosely, Lio-sam-GPS, and Point-LIO fail.

LiDAR degeneracy, it traversed the surroundings and returned to the flat area five times. Upon each return, severe degeneracy occurred in the LiDAR readings, which only captured the flat terrain without any other structures. This sequence includes six times of LiDAR degeneracy and exhibits an average pseudo-range noise level of 2.28 m.

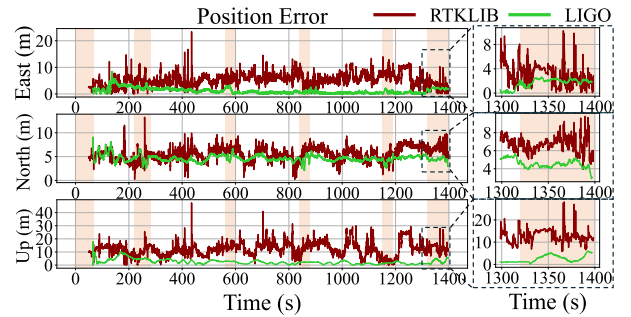


Fig. 5. The trajectory estimation errors along the time after the initial 50s for Deg-2 sequence. Red background indicates time period with LiDAR degeneracy.

Similar to the Deg-1, only LIGO succeeded in producing consistent mapping results and drift-free trajectories for this long-trajectory sequence, while LIGO-loosely, Lio-sam-GPS, and Point-LIO encountered failures. As depicted in Fig. 3, LIGO accurately maps the surrounding buildings without layering issues and exhibits drift-free trajectory estimations in the local-world frame for this long-trajectory movement. Conversely, LIGO-loosely and Point-LIO exhibit drift at the

outset (marked by the red dot in Fig. 3 (e)) of the experiment when the LiDAR is directed towards the flat terrain (illustrated by the pink box in Fig. 3 (b)). Lio-sam-GPS experiences errors also at the beginning of the experiment due to the absence of features for localization.

Fig. 4 compares the estimation trajectories after the initial 50s of LIGO and RTKLIB PPP solutions with the ground truth. Notably, LIGO achieves a horizon RMSE of 4.920m and a total RMSE of 5.795m, outperforming RTKLIB, which records a horizon RMSE of 8.018m and a total RMSE of 15.43m. Despite the multiple times of severe LiDAR degeneracy, LIGO demonstrates superior global localization accuracy compared to RTKLIB.

Fig. 5 provides a temporal overview of the estimation errors after the initial 50s, where the red background signifies the time period with severe LiDAR degeneracy. Notably, LIGO exhibits smoother and smaller error trajectories compared to RTKLIB, owing to the compact LiDAR-Inertial factors it employs. During the occurrence of severe LiDAR degeneracy, LIGO does not show any abnormal estimation errors but works normally and smoothly. This figure further verifies the robustness of LIGO under LiDAR degeneracy and drift-free trajectories in long-trajectory scenarios.

REFERENCES

- [1] F. Pomerleau, F. Colas, R. Siegwart, *et al.*, "A review of point cloud registration algorithms for mobile robotics," *Foundations and Trends® in Robotics*, vol. 4, no. 1, pp. 1–104, 2015.